PNAS RESEARCH ARTICLE | NEUROSCIENCE

SV2A PET reveals synaptic density loss in experimental autoimmune encephalomyelitis and in a pilot multiple sclerosis study

Pou Hong Justin Chia[a,b,1], Takuya Toyonaga[c,1], Junchao Tong[a], Hannah Le[a,b], Mark Dias[c], Amanda J. Boyle[a,b,d], Roger Raymond[a], Erin E. Longbrake[e], Yiyun Huang[c], Richard E. Carson[c], Laura Airas[f], Neil Vasdev[a,d], Ming-Kai Chen[c,2], and Chao Zheng[a,b,d,g,2]

Affiliations are included on p. 10.

Edited by Michael Phelps, David Geffen School of Medicine at UCLA, Los Angeles, CA; received July 3, 2025; accepted January 29, 2026

Synaptic loss is increasingly recognized as a key pathological feature in multiple sclerosis (MS), contributing to disease progression and cognitive dysfunction. Synaptic vesicle glycoprotein 2A (SV2A) positron emission tomography (PET) imaging has emerged as a promising tool for quantifying synaptic density in vivo. Here, we used the clinically translatable tracer [^{18}F]SynVesT-1 to comprehensively characterize synaptic density across the brain and spinal cord in the experimental autoimmune encephalomyelitis (EAE) mouse model of MS. In parallel, we performed SV2A PET in patients with MS using the first clinically implemented SV2A radiotracer, [^{11}C]UCB-J, providing cross-species validation of SV2A PET imaging as a biomarker of synaptic pathology. In EAE mice, dynamic [^{18}F]SynVesT-1 PET imaging revealed a significant global reduction in tracer uptake, with nearly 30% decrease in regional distribution volume (V_T) across all analyzed brain regions ($P < 0.0001$). Correspondingly, autoradiography (ARG) corroborated the PET findings, and additional analyses demonstrated reduced SV2A levels in the cervical and lumbar spinal cord. In a clinical PET research study, [^{11}C]UCB-J imaging in MS patients (n = 6) versus age-matched healthy controls (n = 6) showed a 16.4% reduction in global cortical SV2A binding ($P = 0.026$), with significant regional reductions of 16 to 26% in several cortical and subcortical subregions. Together, these findings demonstrate that SV2A PET imaging provides a sensitive and quantitative biomarker of synaptic pathology in MS. The consistent reductions in SV2A binding observed in both preclinical and clinical research highlight the role of synaptic degeneration in MS and underscore the utility of SV2A PET imaging in MS research.

multiple sclerosis | synaptic density | positron emission tomography | synaptic vesicle glycoprotein 2A | translational

Significance

Synaptic loss is recognized as a major contributor to cognitive decline and long-term disability in multiple sclerosis (MS), yet it remains difficult to measure in vivo. Here, we use synaptic vesicle glycoprotein 2A (SV2A) positron emission tomography (PET) to quantify synaptic density loss across the brain and spinal cord in an experimental autoimmune encephalomyelitis (EAE) mouse model and in patients with MS. In mice, [^{18}F]SynVesT-1 PET reveals widespread reductions in synaptic density corroborated by autoradiography (ARG) and immunofluorescence (IF). Clinically, our pilot study demonstrates the feasibility of using [^{11}C]UCB-J PET to quantify gray-matter synaptic loss in vivo in MS patients. Together, these findings support SV2A PET as a promising translational tool for probing synaptic pathology in MS and for future studies of disease progression and therapeutic interventions.

Multiple sclerosis (MS) is a chronic inflammatory neurodegenerative disease of the central nervous system (CNS), characterized by demyelination, gliosis, and axonal degeneration (1–3). It typically manifests in young adults and follows a variable clinical course, often with periods of relapse and remission. Synaptic loss has recently emerged as a key pathological feature of MS, contributing to irreversible disease progression and long-term neurological deficits (4, 5). This degenerative synaptic pathology is thought to arise when autoimmune cells infiltrate the CNS by crossing the blood–brain barrier (BBB) and attack the myelin sheath, leading to demyelination and subsequent inflammatory responses. These processes trigger glial activation, cytokine release, and excitotoxic damage to synapses, resulting in widespread synaptic density loss (6–10). Specifically, the inflammatory milieu within the CNS is exacerbated by activated macrophages and T cells, which secrete a variety of cytokines and other soluble mediators. These substances compromise the structural integrity of the BBB, facilitating an increased infiltration of immune cells and proinflammatory cytokines into the neural tissue (11). Concurrently, activated astrocytes contribute to the pathological landscape by increasing the production of reactive oxygen species (ROS), which further perpetuate cellular stress and neuronal damage (12). This cascade of biochemical and cellular events creates a highly toxic environment that directly impairs neuronal function and leads to the progressive loss of synaptic density, critically undermining neural connectivity and function (Fig. 1). The resultant synaptic degradation is a primary contributor to the cognitive decline and physical disability observed in MS patients, underscoring the complex interplay between neuroinflammation and neurodegeneration (13, 14).

Experimental autoimmune encephalomyelitis (EAE), the most widely used animal model of MS, recapitulates several key features of the human disease, including

The authors declare no competing interest.

This article is a PNAS Direct Submission.

[1]P.H.J.C. and T.T. contributed equally to this work.

[2]To whom correspondence may be addressed. Email: ming-kai.chen@yale.edu or chao.zheng@camh.ca.

This article contains supporting information online at https://www.pnas.org/lookup/suppl/doi:10.1073/pnas.2517709123/-/DCSupplemental.

Published March 3, 2026.

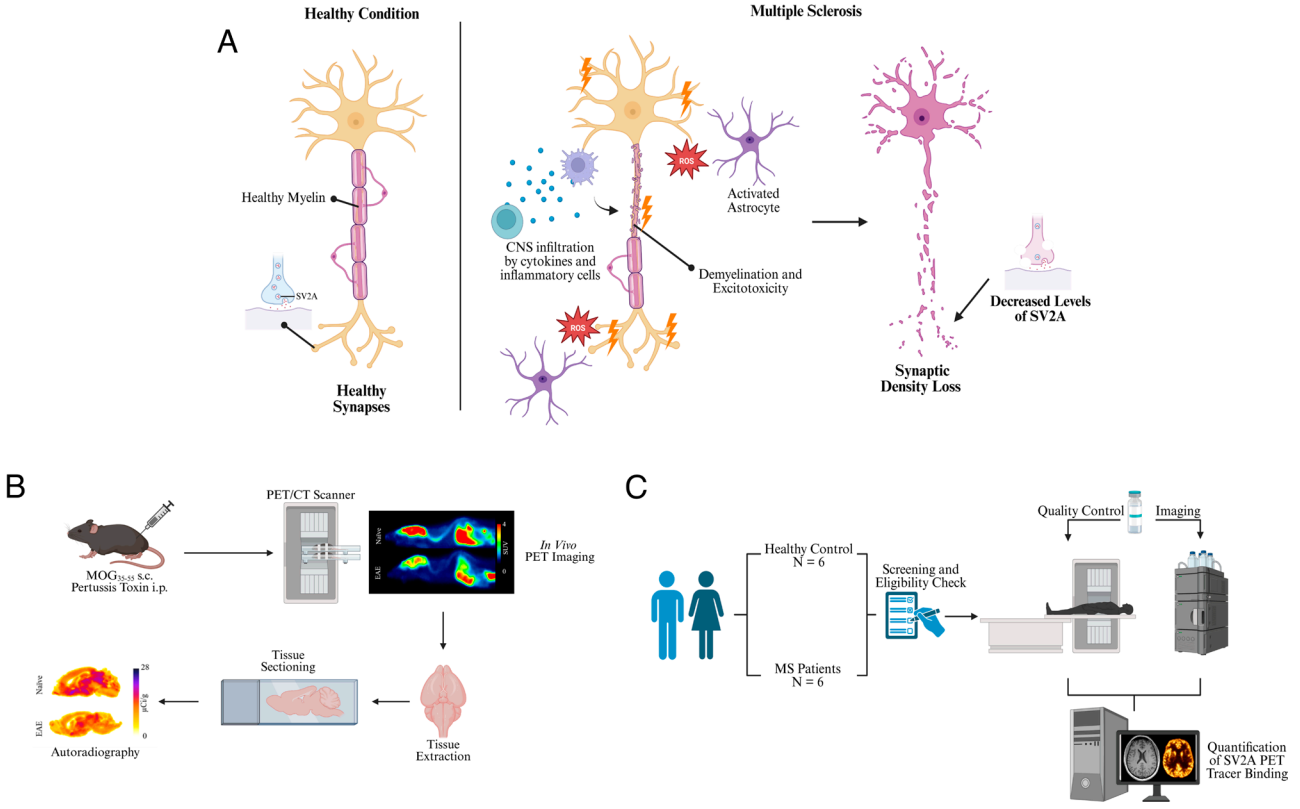

Fig. 1. Theoretical cellular mechanisms of synaptic loss and general experimental design for SV2A imaging in MS patients and EAE mice. (*A*) Illustration of the cellular mechanisms contributing to synaptic damage in MS. The diagram shows cytokines and inflammatory cells infiltrating the CNS and triggering demyelination. This leads to the activation of astrocytes and the production of ROS, which contribute to oxidative stress, more demyelination, and neuronal dysfunction. The loss of myelin impairs axonal transport and synaptic vesicle recycling, possibly reducing SV2A expression and neurotransmitter release, ultimately leading to synaptic degeneration. (*B*) Experimental workflow for SV2A imaging in EAE mice. EAE was induced in C57BL/6J mice and scanned only upon reaching a clinical score of ≥3 (n = 18/group). Following imaging, brains were extracted, sectioned, and subjected to autoradiography (ARG) for SV2A quantification (n = 6/group). Representative PET and ARG images of SV2A binding in naïve and EAE mouse are shown. (*C*) Workflow for the human imaging study. Healthy controls and MS patients underwent screening and eligibility assessment before PET imaging. Imaging included quality control and patient-based radiometabolite correction before quantification of SV2A binding.

neuroinflammation, demyelination, and axonal damage (10, 15, 16). In EAE mice, excitatory synapses have been shown to destabilize and degrade, disrupting neuronal connectivity and promoting disease progression (17). Postmortem human studies similarly demonstrate substantial synaptic loss in various regions of the brain through immunohistochemical analyses (8, 18–21). Notably, recent evidence suggests that synaptic alterations occur independently of demyelination and axonal degeneration, with synaptic loss detected in the gray matter of MS brains and EAE models even before clinical symptoms or disease onset (22, 23). These findings highlight the pivotal role of synaptic loss in the pathogenesis of MS and suggest that effective synaptic biomarkers could be crucial for both diagnosis and the development of novel therapeutic strategies.

Currently, MRI is the gold-standard diagnostic tool for MS and disease monitoring, providing detailed structural information on demyelinating lesions and brain atrophy (24, 25). However, MRI is limited in its ability to capture early molecular and cellular changes, such as synaptic loss, which drive disease progression (26–28). Additionally, MRI-derived measures often correlate poorly with clinical symptoms, particularly in progressive stages of MS (29). These clinical challenges highlight the need for complementary imaging methods to investigate synaptic pathology and improve our understanding of MS. Positron emission tomography (PET), on the other hand, offers unique advantages for studying biochemical and cellular processes in vivo (30–32). In the context of MS, [^{18}F]FDG remains the most widely applied PET radiopharmaceuticals in clinical settings, primarily reflecting regional glucose metabolism and neuronal dysfunction (33). Other PET radiopharmaceuticals such as those targeting translocator protein 18 kDa (TSPO) for microglial activation (e.g., [^{11}C]PK11195, [^{18}F]DPA714) and the amyloid imaging agent [^{11}C]PiB as a surrogate measure of myelin content have shown some promise in clinical research in MS (4, 34). Despite these advances, reliable in vivo quantification of neuronal and synaptic integrity in MS remains a critical unmet need in understanding disease progression and monitoring treatment response. Among the molecular targets for PET imaging, synaptic vesicle glycoprotein 2A (SV2A) has been validated as a robust biomarker of synaptic density due to its ubiquitous expression in presynaptic terminals and critical role in neurotransmitter release (4, 35). Recent development of high-affinity SV2A PET tracers, including [^{11}C]UCB-J (26, 36–38), [^{11}C]UCB-A (39), [^{18}F]UCB-H (40, 41), [^{18}F]SynVesT-1/2 (42–44), and [^{18}F]SDM-16 (45, 46), has enabled specific and sensitive quantification of synaptic density in various neurological disorders, including Alzheimer's disease and spinal cord injury (21, 43, 46–50). Although emerging SV2A PET studies in a cortical MS mouse model and in patients with MS have begun to implicate synaptic alterations in demyelinating pathology (28, 51), synaptic density has not yet been systematically evaluated along the entire CNS axis, including both the brain and spinal cord.

Here, we applied SV2A PET imaging using [^{18}F]SynVesT-1 to quantify synaptic density across the entire CNS in the EAE mouse

model of MS. Given the established EAE pathology in the spinal cord and the potential of SV2A PET tracers for imaging spinal synaptic damage, we explicitly assessed changes in SV2A density within the rodent spinal cord in addition to the brain (18, 52, 53). Postmortem SV2A measurements in mouse brain tissues were conducted to corroborate the in vivo PET imaging findings. In parallel, to establish the translational relevance of these observations, we conducted an exploratory SV2A PET imaging study in patients with MS using [^{11}C]UCB-J, the first-in-human SV2A tracer and current clinical gold standard for synaptic quantification, to provide a robust biological benchmark against which our preclinical findings could be contextualized (Fig. 1) (54, 55).

Materials and Methods

Animals and Experimental Design. All experiments were conducted in accordance with the guidelines established by the institutional animal care and use committee at the Centre for Addiction and Mental Health (CAMH). EAE was induced in C57BL/6J mice (n = 18, 10F + 8M) via subcutaneous immunization with Myelin Oligodendrocyte Glycoprotein$_{35–55}$ (MOG$_{35–55}$) peptide in complete Freund's adjuvant, followed by intraperitoneal pertussis toxin injections using a commercially available EAE induction kit (Hooke Laboratories, catalog number EK-2110). Mice (9 to 13 wk old) were group-housed in temperature- and humidity-controlled environments with food and water. They were maintained under a 12-h light/dark cycle to minimize stress prior to and during the experimental period. Clinical EAE scores were recorded daily from the day of immunization. Mice were observed for the onset of clinical signs, with typical disease development beginning between 9- and 14-d postimmunization. Experiments were then conducted when the mice reached an EAE score of 3 or higher in this study. Naïve controls (n = 18, 10F + 8 M) were subjected to the same handling and experimental conditions as the EAE group but did not receive any immunization or injections. Animals were killed at the experimental endpoint for histological analysis. The expected clinical progression followed a typical chronic-relapsing EAE course, characterized by tail limpness, hind limb weakness, and eventual partial recovery, with clinical scores ranging from 0 to 5, where 0 indicates no clinical symptoms, and 5 represents severe paralysis or moribundity.

Small-Animal PET Scanning with [^{18}F]SynVesT-1. [^{18}F]SynVesT-1 was synthesized following previously published methods (42, 43, 48, 49, 56). Dynamic PET/computed tomography (CT) imaging was performed using [^{18}F]SynVesT-1 in EAE mice (n = 18) and their corresponding naïve controls (n = 18). All mouse imaging studies were conducted in accordance with the guidelines established by the institutional animal care and use committees at CAMH. Mice were anesthetized using isoflurane in O_2 (4%, 2 L/min for induction; 1.5 to 2%, 1 L/min for maintenance) for lateral tail-vein catheterization and subsequently transferred to a nanoScan PET/CT scanner (Mediso, Budapest, Hungary) using a quad-mice pallet. Anesthesia was maintained throughout the imaging session, with body temperature and respiratory parameters monitored closely for each mouse. A scout CT scan was performed for positioning the PET field of view (FOV), followed by a material map CT acquisition for attenuation and scatter corrections using a segmented material map and for PET/CT coregistration. A bolus injection of [^{18}F]SynVesT-1 was administered via the tail-vein catheter, and dynamic PET images were acquired over a 90-min period to assess tracer uptake and distribution.

Image Processing and Analysis for Rodent Scans. A static image of the entire 90-min emission acquisition was reconstructed using the manufacturer's proprietary iterative three-dimensional (3D) algorithm (six subsets and four iterations) for coregistration with the CT scan, while dynamic images were reconstructed using both 2D-filtered back projection (FBP) and 3D-iterative (six subsets and four iterations) algorithms. The analytically reconstructed image was used for regional brain time-activity curve (TAC) extraction and the iteratively reconstructed image was used for manual spinal cord and cardiac blood pool TAC by manually drawing a ROI over the spinal cord and the left ventricle of the heart, guided by the CT image. The cardiac blood pool TAC was then used to obtain radiometabolite-corrected image-derived input functions (IDIF) in plasma based on a recent publication by Bertoglio 2022 in C57BL/6J mice. The dynamic dataset consisted of 39 frames: 3 × 5 s, 3 × 15 s, 3 × 20 s, 7 × 60 s, 17 × 180 s, and 6 × 300 s. Brain regions of interest (ROIs) for PET imaging were defined by coregistering PET images with a mouse brain MRI atlas (57). Spinal cord regions of interest (cervical, thoracic, lumbar, and sacral) were manually defined on coregistered CT images guided by a CT atlas (58). The standardized uptake values (SUVs) were calculated by normalizing the regional radioactivity to the injected dose and body weight of each mouse. The standardized uptake value ratio (SUVR) was further calculated by dividing the SUV of the ROI by the SUV of a reference region. One-tissue compartmental model (1TCM), two-tissue compartment model (2TCM), and Logan plot with plasma IDIF were used for kinetic modeling in PMOD (ver. 4.203, Zurich, Switzerland). The distribution volume in mL/cm^3 (V_T) was reported with radiometabolite-correction as described previously (59). The distribution volume ratio (DVR) was derived using the Logan reference tissue model. Voxel-wise comparisons of spatially between naïve and EAE mouse groups were conducted using MATLAB R2024b (MathWorks) and Statistical Parametric Mapping (SPM12). Logan Plot–derived V_T maps were resliced, and two-sample Student's t tests were performed using 1 –1 contrast with no explicit masking. Statistical significance at each voxel was defined as $p < 0.001$ and corrected for multiple comparisons using family-wise error (FWE) correction. The resulting t-maps were overlaid onto the MRI brain mouse template for visualization.

In Vitro and Ex Vivo Autoradiography Using [^{18}F]SynVesT-1. Brain and spinal cord tissues were freshly extracted from anesthetized mice (under isoflurane) and immediately frozen at –80 °C until cryostat sectioning. Frozen tissues were embedded in Tissue-Tek O.C.T. (Sakura Finetek, Tokyo, Japan). For the brain, serial 10 μm-thick sagittal sections of the left hemisphere were generated using a Cryostar NX50 cryostat (Thermo Fisher Scientific, Runcorn, UK) and stored at –80 °C. For the spinal cord, coronal sections (10 μm-thick) were generated using the same cryostat. These sections were carefully separated and pooled based on the anatomical location of the butterfly gray matter shape into cervical, thoracic, and lumbar segments for regional analysis, and then stored at –80 °C until biological assays were performed. Autoradiography (ARG) was performed on tissue sections obtained from mice in the naïve and EAE groups, with all cohorts being sex balanced. For the brain ARG analysis, tissue sections were utilized from twelve mice in total (N = 6 naïve, N = 6 EAE, sex balanced). For the spinal cord ARG analysis, tissue sections were utilized from a subset of eight mice in total (N = 4 naïve, N = 4 EAE, sex balanced). Tissue slices were incubated with [^{18}F]SynVesT-1 (10 μCi/mL). Blocking was performed using 200 μM Levetiracetam (LEV), a known antiepileptic drug targeting SV2A (60). Following incubation, sections were rinsed twice for 1 min in rinse buffer at 4 °C, followed by a 10-sec rinse in ice-cold distilled water. Slides were dried under airflow for 5 min before being exposed to a storage phosphor (SR) screen for 30 min. To confirm the regional distribution of tracer retention postinjection (*p.i.*), ex vivo ARG was performed on a separate subset of mice (N = 4, 2 M + 2F, naïve; N = 5, 3M + 2F, EAE). Animals were killed immediately following the completion of the 90-min dynamic PET scan. Brains were rapidly extracted, frozen, and sectioned as described above. These sections were then exposed directly to an SR screen for 30 min immediately to capture the in vivo tracer profile.

ARG Imaging and Quantification. All autoradiographic images were acquired using an Amersham Typhoon™ Biomolecular Imager (GE Healthcare, MA) at 25 μm resolution. For quantification, ten [^{18}F]SynVesT-1 standards were counted using a gamma counter (PerkinElmer, Waltham, MA) and decay-corrected to the exposure time. For in vitro analysis, specific binding was calculated by subtracting nonspecific binding from total binding, with results expressed in μCi/mg based on the calibration standards. Regional quantification was performed using MCID Core 7 (Interfocus Imaging Ltd.). To ensure valid data comparison for the ex vivo analysis, final tissue radioactivity values were normalized to the injected dose and body weight of each animal.

Immunofluorescence (IF) Staining on the EAE Mice Brain and Spinal Cord. Fresh-frozen sagittal brain and coronal spinal cord sections (10 μm) were brought to room temperature and postfixed in 4% paraformaldehyde for 20 min. Following three washes in phosphate-buffered saline (PBS; pH 7.4), heat-induced antigen retrieval was performed in sodium citrate buffer (10 mM, pH 6.0) at 60 °C for 45 mins. Sections were washed and incubated for 1 h in a blocking solution containing 5% normal donkey serum and 0.3% Triton X-100 in PBS. Primary incubation was carried out overnight at 4 °C with rabbit anti-SV2A (1:500; Abcam, ab32942) diluted in blocking solution. Following PBS washes, sections

Table 1. Demographic and clinical characteristics of study participants

	Healthy control	Multiple sclerosis
Participants	6	6 (5 RRMS, 1 SPMS)
Sex (M/F)	4/2	1/5
Age (years)	48.8 (7.6) (39–61)	48.1 (7.1) (39–59)
Years since MS diagnosis (years)	–	14.5 (11.7) (4–37)
Medication	–	Tecfidera (4), Copaxone (1), Rituxan (1)
EDSS	–	4 (2.0 to 6.5)
^{11}C-UCB-J (MBq)	528 (191)	599 (183)

Summary of participant characteristics for the healthy control and MS groups. The MS cohort includes 5 participants with relapsing-remitting MS (RRMS) and 1 with secondary progressive MS (SPMS). Data are presented as mean (SD) with range in parentheses where applicable. MS duration (years) and Expanded Disability Status Scale (EDSS) scores are provided for the MS group. Note that EDSS was reported as median with range in parentheses. Injected dose of [^{11}C]UCB-J is reported in megabecquerels (MBq).

were incubated for 2 h with donkey anti-rabbit Alexa Fluor Plus 488 (1:500; Invitrogen) diluted in blocking solution. Nuclei were counterstained with DAPI (1:5,000; Roche Diagnostics) for 3 min. Sections were mounted using Prolong Gold antifade media (Invitrogen). Whole-slide images were acquired using an Olympus VS200 slide scanner at 10x magnification. Quantitative analysis was performed using ImageJ (NIH). To quantify SV2A density, images were normalized for brightness and contrast, converted to 8-bit grayscale, and binarized. To account for slight technical variations in staining intensity between sections, the lower intensity threshold was individually calibrated using the white matter as an internal background reference. The threshold cutoff was set to the specific level required to eliminate nonspecific signal in the white matter tracts (Range: 27 to 255), ensuring that only specific gray matter immunoreactivity was included in the analysis. SV2A fractional area was quantified within manually defined regions of interest (ROIs). Data are expressed as the percentage of area positively stained for SV2A.

Human Subjects. This study included six individuals with MS and six age-matched healthy controls (Table 1). MS participants were aged 18 to 60, met the revised McDonald criteria for a definite diagnosis, and had an Expanded Disability Status Scale (EDSS) score between 0 and 7.5. Healthy controls were aged 18 to 65, matched to MS participants for age, and had normal physical exams, EKG, and blood tests. Exclusion criteria for all participants included prior/current radiation exposure exceeding FDA limits, blood donation within eight weeks, MRI contraindications, other neurological disorders mimicking MS, pregnancy/lactation, chronic corticosteroid/immunosuppressant use, active/chronic infections, progressive multifocal leukoencephalopathy, renal impairment, and bleeding disorders/anticoagulant use. The study protocol was approved by the Yale University Human Investigation Committee and the Yale New Haven Hospital Radiation Safety Committee and adhered to 45 CFR 46, the US federal regulations for human research protection. All participants provided written informed consent after receiving a thorough explanation of the study procedures (Fig. 1).

Human PET Imaging Study With [^{11}C]UCB-J. [^{11}C]UCB-J was synthesized following previously published methods (54). All participants underwent a single [^{11}C]UCB-J dynamic PET scan using the Siemens High Resolution Research Tomograph (HRRT; Siemens, Medical Solutions, Knoxville, TN) with a reconstructed image resolution of approximately 3 mm. PET imaging procedures were conducted as previously described (61, 62). All participants also underwent T1-weighted MRI on a 3-T whole-body scanner (Trio, Siemens) for subsequent coregistration with the PET images. PET images were aligned to individual MR images through rigid registration. Subsequently, individual MR images were normalized to Montreal Neurological Institute space using affine linear and nonlinear registration within the BioImage Suite 2.5 software. Regions of interest (ROIs) were then extracted from the automated anatomic labeling (AAL) template.

Quantitative Analysis for Human Scan. Kinetic analysis was performed on the regional time activity curves (TACs) using the one-tissue compartment model (1TCM) (61) and the metabolite-corrected arterial plasma curve to generate parametric images of V_T. V_T represents the tissue-to-plasma concentration ratio at equilibrium and reflects both specific and nonspecific binding. 18 anatomically defined ROIs were applied to the PET images using the combined transformations derived from the template-to-PET image space. The spinal cord was defined by referring 0 to 90 min summed image and manually draw in 15 slices from the end of medulla to posterior. Volume-weighted averages were also calculated for entire cortical ROIs, encompassing the frontal, temporal, parietal, and occipital lobes, as well as the insula and cingulate cortex.

Statistical Analysis. Data were analyzed using GraphPad Prism (version 10). For preclinical animal studies, differences in quantitative PET metrics (V_T, SUVR, DVR, K_1) and in vitro measures between naïve and EAE mice across multiple brain and spinal cord regions were assessed using an ordinary two-way ANOVA. Post hoc pairwise comparisons were corrected for multiple comparisons using Sidak's multiple comparisons test. For human data, two-tailed, unpaired Welch's *t* tests were used to compare regional V_T of [^{11}C]UCB-J between MS and healthy control (HC) participants. Due to the small sample size, no correction for multiple comparisons was applied.

Result

PET Imaging Reveals Decreased [^{18}F]SynVesT-1 Brain Uptake in EAE Mice. All naïve and EAE mice received a single injection of [^{18}F]SynVesT-1 (7.03 ± 0.88 MBq). Compared with naïve controls, EAE mice showed visibly reduced tracer uptake throughout the brain (Fig. 2*A* and *SI Appendix*, Fig. S7*A*). This reduction was also reflected in the TACs, lower SUVs in all examined regions, particularly during the first 30 min *p.i.* (Fig. 2 *B* and *C*). To further substantiate these observations, we performed semiquantitative analysis using the amygdala as a pseudoreference region, selected due to its relatively stable uptake across groups (*SI Appendix*, Fig. S8). During the stable late-acquisition window (60 to 90 min), SUVRs were significantly reduced in all major brain regions of EAE mice (*SI Appendix*, Fig. S8*D*).

Decrease in Synaptic Density in EAE Mice Through PET Imaging. To rigorously quantify SV2A density in vivo, we estimated total V_T (mL/cm^3) using an IDIF in naïve and EAE mice (Fig. 3, *SI Appendix*, Table S1). Satisfyingly, regional TACs were adequately described by both 1TCM and 2TCM compartment models. Although the two approaches yielded comparable V_T values (*SI Appendix*, Fig. S2*A*), the 2TCM was statistically preferred based on goodness-of-fit parameters, including the Model Selection Criterion (MSC) and Akaike Information Criterion (AIC) (*SI Appendix*, Tables S2 and S3). Importantly, V_T estimates derived from the 2TCM were highly consistent with those obtained using Logan graphical analysis (Fig. 3*A*). Given this concordance, together with the greater numerical stability of linear methods, final V_T values were derived using the Logan plot to ensure robust quantification.

To exclude potential confounding effects of altered radiotracer metabolism in EAE mice, we compared V_T values calculated with and without population-based radiometabolite correction; regardless of the method used, V_T estimates were strongly and significantly correlated ($R^2 > 0.9$) (Fig. 3*A* and *SI Appendix*, Fig. S2*B*), indicating that potential alterations in peripheral metabolism may not drive the observed group effects. V_T values obtained with Logan analysis using two different t^* settings were also highly consistent, with no systematic deviation (*SI Appendix*, Fig. S2*C*). To visualize the spatial extent of pathology, we generated group-averaged Logan V_T parametric images (t^*= 9 min), which revealed an apparent global reduction in tracer uptake in EAE mice (Fig. 3*B*). This was confirmed by voxel-wise *t*-statistics analysis, demonstrating widespread significant V_T decreases throughout the brain parenchyma (*SI Appendix*, Fig. S3). We then

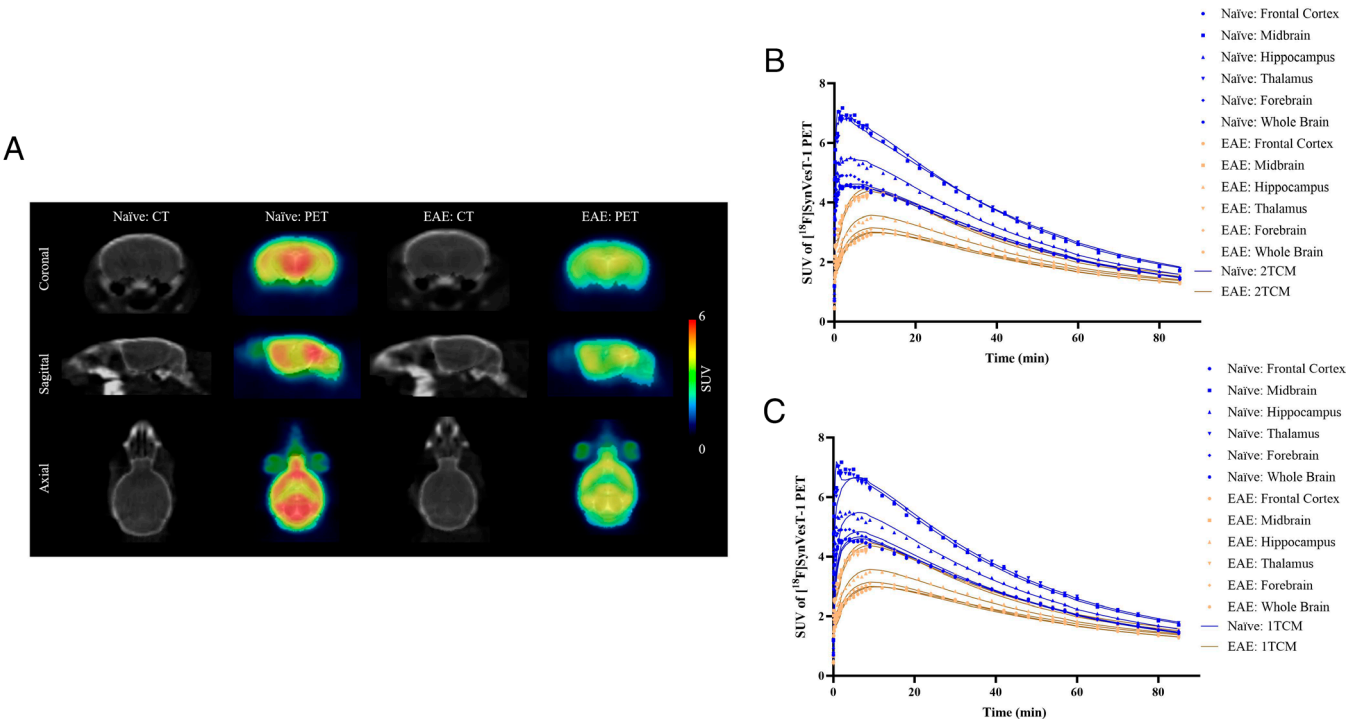

Fig. 2. [^{18}F]SynVesT-1 uptake is reduced in EAE mice. (*A*) Representative CT and PET SUV (0 to 90 mins *p.i.*) images of [^{18}F]SynVesT-1 in naïve and EAE mice and the overlaid image with an MRI mouse brain atlas. Scale bar represents SUV value. (*B*) Regional time activity curves (TACs) for the frontal cortex, midbrain, hippocampus, thalamus, forebrain, and whole brain in naïve (blue) and EAE (orange) mice with 2TCM model fits (solid lines). (*C*) Regional TACs for the frontal cortex, midbrain, hippocampus, thalamus, forebrain, and whole brain in naïve (blue) and EAE (orange) mice with 1TCM model fits (solid lines).

compared regional V_T values across various brain regions, selected for their involvement in EAE and MS (63, 64). Both kinetic models revealed significant reduction in [^{18}F]SynVesT-1 uptake across all analyzed regions (Fig. 3 *C* and *D* and *SI Appendix*, Table S1). Using Logan-derived V_T, EAE mice showed significantly reduced in the caudate putamen (–25.2%, $P < 0.0001$), frontal cortex (–26.0%, $P < 0.0001$), nucleus accumbens (–24.7%, $P < 0.0001$), hippocampus (–26.5%, $P < 0.0001$), thalamus (–26.7%, $P < 0.0001$), forebrain (–26.6%, $P < 0.0001$), and whole brain (–27.9%, $P < 0.0001$).

[^{18}F]SynVesT-1 PET Imaging Reveals Synaptic Density Loss in the Spinal Cord in EAE Mice. Leveraging the ability of PET imaging to interrogate spinal cord pathology, we next assessed SV2A changes along the spinal axis in EAE mice. The specificity of [^{18}F]SynVesT-1 binding in the spinal cord was first confirmed in vivo by a blocking study (*SI Appendix*, Fig. S1), in which pretreatment with LEV significantly reduced tracer uptake in the cervical, thoracic, and lumbar segments (*SI Appendix*, Fig. S1*E*). In the EAE cohort, qualitative PET images suggested lower [^{18}F]SynVesT-1 uptake, most prominently in the cervical and lumbar segments (Fig. 4*A*), an impression supported by regional TACs showing a downward trend in SUV in these regions (Fig. 4*B*). For quantitative analysis, we calculated SUVR values from 60 to 90 min *p.i.* using the sacral spinal cord as a pseudoreference region. SUVRs were significantly reduced in the cervical (–15.7%, $P < 0.05$) and lumbar (–15.4%, $P < 0.01$) segments, whereas thoracic SUVR remained unchanged (Fig. 4*C*). Absolute V_T values derived from Logan graphical analysis with a corrected IDIF showed a similar pattern, with robust V_T decreases in the cervical (–27.7%, $P < 0.0001$) and lumbar (–21.7%, $P < 0.01$) spinal cord and no significant change in the thoracic segment (Fig. 4*D*). Consistently, DVR estimates calculated using the sacral as the pseudoreference also demonstrated significant reductions in cervical (–16.5%, $P < 0.01$) and lumbar (–16.0%, $P < 0.05$) segments, with thoracic DVR unchanged (Fig. 4*E*). Together, the concordant SUVR, V_T, and DVR findings indicate a segment-specific reduction of SV2A signal in EAE mice, with the cervical and lumbar spinal cord preferentially affected.

Postmortem In Vitro and Ex Vivo Analysis Corroborates SV2A Reduction in the EAE Mice Brain and Spinal Cord. To corroborate the in vivo [^{18}F]SynVesT-1 PET findings at the cellular level, we performed postmortem in vitro ARG and IF staining for SV2A on sagittal brain and coronal spinal cord sections from EAE and naïve control mice (Fig. 5 and *SI Appendix*, Fig. S6). Binding specificity of [^{18}F]SynVesT-1 in postmortem tissue was confirmed by in vitro ARG, which showed that 84.4 ± 0.4% and 83.7 ± 0.6% of total binding was displaceable in the brain and spinal cord, respectively (Fig. 5*A* and *SI Appendix*, Fig. S5*C*), consistent with a high degree of specific SV2A binding. In line with the in vivo PET imaging results, [^{18}F]SynVesT-1 specific binding was significantly reduced in the cerebellum (–20.7%, $P < 0.001$), cerebral cortex (–15.9%, $P < 0.05$), and midbrain (–9.99%, $P < 0.05$) (Fig. 5*B*), with the corresponding ROIs used for quantification illustrated in *SI Appendix*, Fig. S5*A*. Significant decreases in tracer binding were also observed in the cervical (–20.8%, $P < 0.05$) and lumbar (–26.3%, $P < 0.05$) spinal cord (Fig. 5 *C* and *D*). These regional reductions in ARG binding were corroborated by IF, which revealed significant parallel reductions in SV2A protein density in the cerebellum (–23.9%, $P < 0.05$) and frontal cortex (–18.7%, $P < 0.05$), as well as in the cervical (–17.7%, $P < 0.01$) and lumbar (–14.2%, $P < 0.05$) spinal cord (*SI Appendix*, Fig. S6 *B* and *D*). Notably, IF detected a significant reduction in hippocampal SV2A staining (–19.9%, $P < 0.05$), whereas the corresponding decrease in in vitro ARG binding did not reach statistical significance. In addition, ex vivo

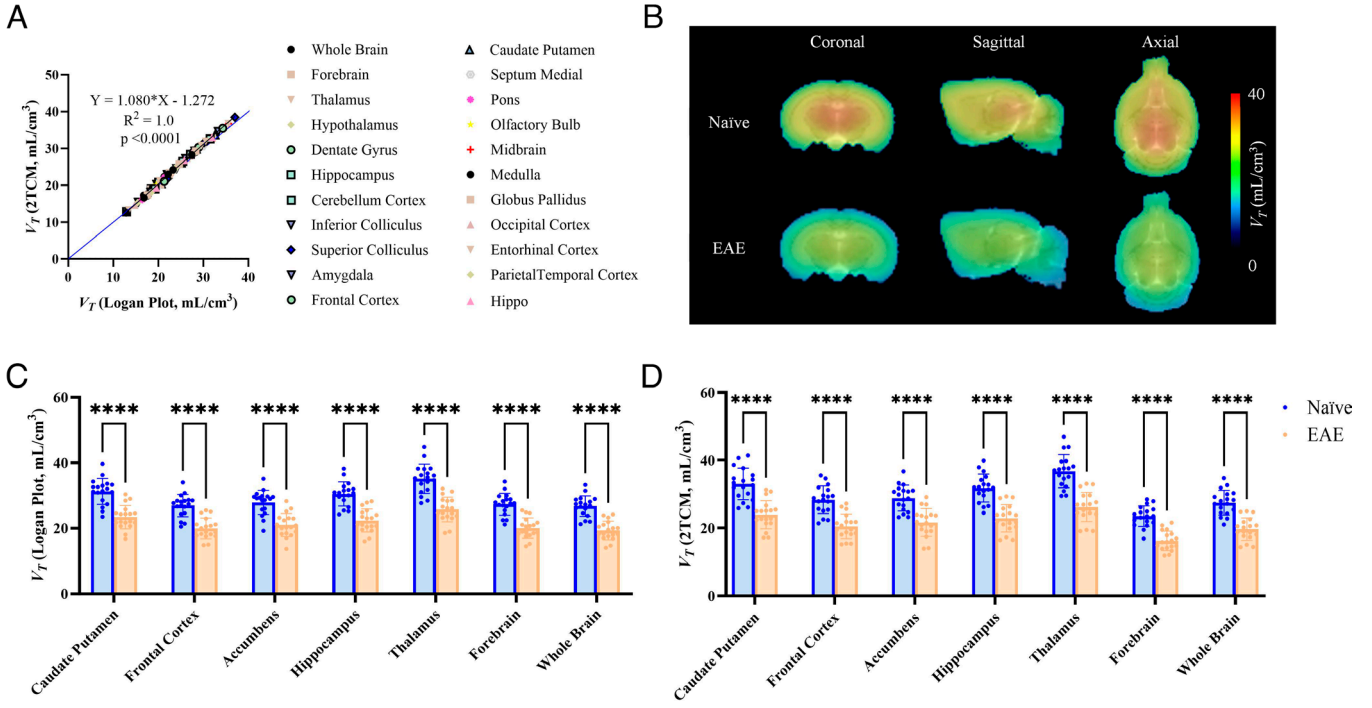

Fig. 3. [^{18}F]SynVesT-1 binding is reduced in EAE mice. (*A*) Correlation between V_T values estimated by the radiometabolite-corrected Logan plot and the 2TCM across brain regions, showing a strong linear relationship (n = 4, R^2 = 1, P < 0.0001). Blue line represents the line of identity. (*B*) Averaged parametric images of V_T derived from radiometabolite-corrected Logan Plot, shown in coronal, sagittal, and axial views. The color scale represents V_T values (mL/cm^3). (*C*) Regional V_T values derived from the Logan plot, demonstrating a significant reduction in [^{18}F]SynVesT-1 binding in multiple brain regions of EAE mice compared to naïve controls (n = 18/group). (*D*) Regional V_T values estimated by the 2TCM, confirming reduced tracer binding in EAE mice (n = 18/group). Data are presented as mean ± SD; ****P < 0.0001.

ARG on brain tissues collected immediately after PET imaging showed strong concordance between in vivo tracer distribution and regional binding at the whole-brain level (*SI Appendix*, Fig. S7).

PET Imaging Reveals Decreased SV2A Tracer Brain Uptake in MS Patients. Building on promising results from preclinical animal studies, we also compared our findings with preliminary human data in MS patients using [^{11}C]UCB-J, the first SV2A tracer employed in clinical research. The study involved six individuals diagnosed with MS and six healthy controls (HC). All participants received a single injection of [^{11}C]UCB-J (528 ± 191 MBq). There was no significant difference in injected doses between groups (MS: 599 ± 183 MBq; HC: 458 ± 187 MBq; P = 0.35) (Table 1). Arterial input functions were obtained in

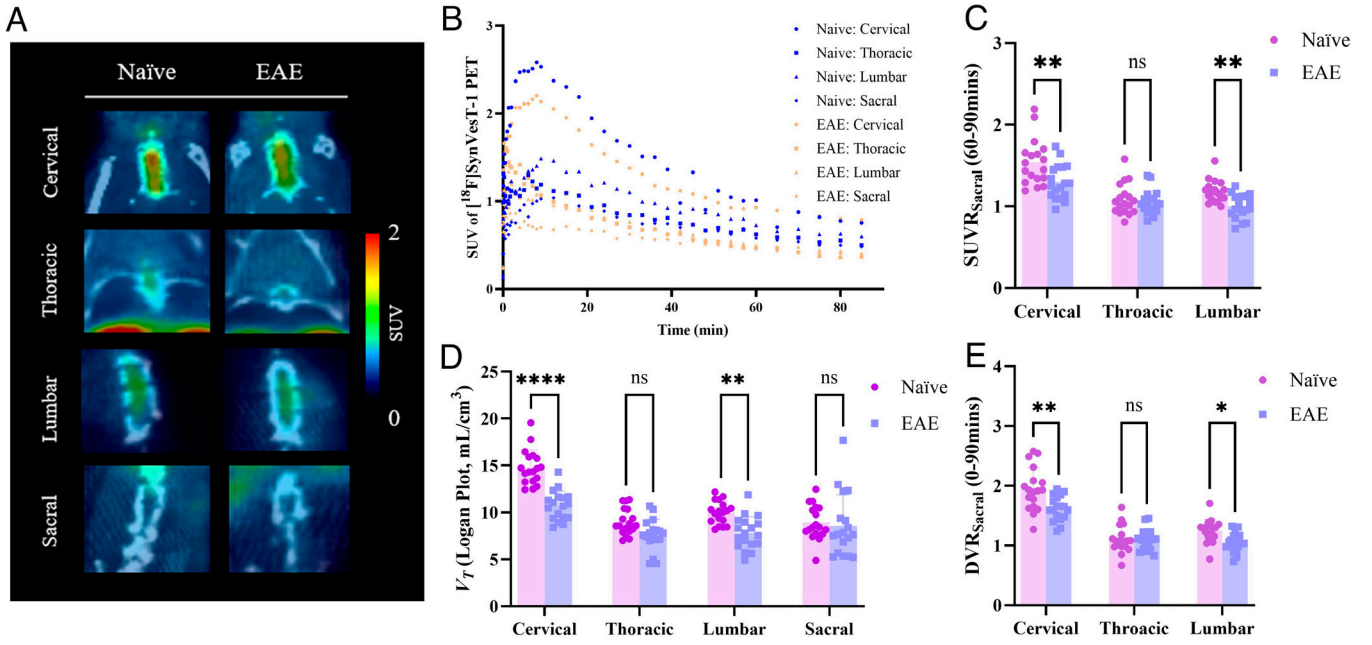

Fig. 4. [^{18}F]SynVesT-1 uptake is reduced in the spinal cord of EAE mice. (*A*) Representative summed PET images (0 to 60 mins *p.i.*) of [^{18}F]SynVesT-1 uptake in the cervical, thoracic, lumbar and sacral spinal cord regions of naïve and EAE mice. The color scale reflects SUV values. (*B*) TACs of [^{18}F]SynVesT-1 SUV in the cervical, thoracic, lumbar and sacral spinal cord regions over 90 min, showing observable reduced tracer uptake in EAE mice. (*C*) Regional SUVR values (60 to 90 min) values normalised to sacral spinal cord uptake. (*D*) Regional V_T values derived from the radiometabolite-corrected Logan plot. (*E*) DVR values derived from Logan Reference Model using the sacral segment as the reference region. Data are presented as mean ± SD (n = 18/group). *P < 0.05, **P < 0.01, ***P < 0.001, ns = not significant.

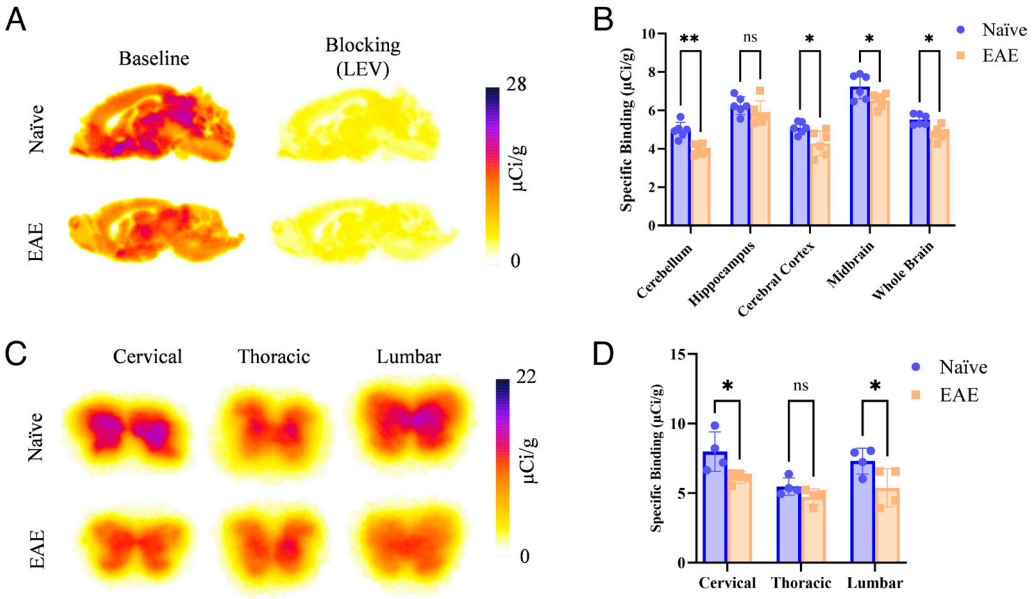

Fig. 5. Postmortem quantification reveals reduced SV2A binding in EAE mice. (*A*) Representative ARG images of [^{18}F]SynVesT-1 binding in the sagittal brain sections of naïve and EAE mice. Scale bar represents binding in µCi/g. (*B*) Regional analysis of specific binding demonstrates a significant reduction in the cerebellum, cerebral cortex, midbrain and whole brain of EAE mice, while hippocampal binding remains unchanged (n = 6/group, 3M + 3F/group). (*C*) Representative ARG images of [^{18}F]SynVesT-1 binding in the coronal spinal cord sections of naïve and EAE mice. Scale bar represents binding in µCi/g. (*D*) Regional analysis of specific binding in the cervical, thoracic and lumbar sections in naïve and EAE mice (n = 4, 2M + 2F/group). Data are presented as mean ± SD. *P < 0.05, ***P < 0.001, ns = not significant.

all participants (6 MS, 6 HC) for V_T measurement (Fig. 6). The primary study revealed a statistically significant 16.4% reduction in [^{11}C]UCB-J binding (V_T) in the cortical regions of MS participants compared to HC (P = 0.026), suggesting widespread loss of SV2A and synaptic density (Fig. 6*B*). Exploratory analyses demonstrated an overall decrease in [^{11}C]UCB-J binding across most examined regions in MS participants, with statistically significant reductions observed in the caudate (–26.0%, P = 0.011), ventral striatum (–18.9%, P = 0.008), thalamus (–19.4%, P = 0.022), frontal cortex (–15.3%, P = 0.038), orbitofrontal cortex (–15.8%, P = 0.039), parietal cortex (–16.3%, P = 0.017), occipital cortex (–18.6%, P = 0.007), and temporal cortex (–16.2%, P = 0.034). There is no significant difference in the spinal cord; however, a 20% difference in V_T was observed between HC and MS participants (Fig. 6*C*). In addition, we examined regional gray matter volumes using FreeSurfer v6.0.0. Although smaller gray matters were seen in the MS participants, no significant group differences were observed (*SI Appendix*, Fig. S10). It is important to note that these preliminary results were not corrected for multiple comparisons due to the small sample size.

Discussion

This study assessed the potential of using the SV2A PET radiopharmaceutical [^{18}F]SynVesT-1 to image synaptic density loss in EAE mice at the peak, clinically relevant stage of disease progression (EAE score ≥ 3). Synaptic density loss is a key hallmark of MS (17, 63, 64). Despite increasing interest in synaptic pathology in EAE and in patients with MS, in vivo imaging markers of synaptic density loss have only recently begun to emerge. Using the SV2A tracer [^{11}C]UCB-J, clinical PET studies have demonstrated measurable reductions in synaptic density in patients with MS, providing noninvasive evidence that SV2A PET reflects neurodegenerative burden in this disease (51). In parallel, studies employing [^{18}F]UCB-H in both a cortical MS model and human cohorts have corroborated these findings, showing that PET-defined synaptic pathology extends far beyond MRI-visible lesion burden and scales with disease progression and disability (28). The present work provides a demonstration of SV2A level changes tracked by [^{18}F]SynVesT-1 PET imaging in EAE mice across the entire CNS, including the brain and spinal cord. Importantly, these preclinical findings were supported by parallel pilot data from MS patients imaged with [^{11}C]UCB-J, the first-in-human SV2A PET tracer and clinical benchmark for SV2A quantification, thereby offering cross-species validation and further supporting the utility of SV2A PET imaging as a robust biomarker of synaptic pathology in the human disease.

In EAE mice, we observed a significant global reduction in SV2A levels at peak disease onset using [^{18}F]SynVesT-1 PET, with nearly 30% loss in all analyzed regions, reinforcing the concept that synaptic pathology is a pervasive feature of MS that can be captured in vivo. Although isoflurane anesthesia has been reported to potentially influence SV2A radiotracer binding (65), the use of identical anesthesia protocols in both naïve and EAE cohorts minimizes its confounding impact on group comparisons. Satisfyingly, our V_T estimates in naïve mice were largely consistent with previously reported V_T values in healthy wild-type mice, with similar regional distributions and only minor differences (66). However, interpretation of V_T in the EAE model of mice requires consideration of disease-related physiological changes. EAE is characterized by BBB disruption, inflammatory vasodilation, and altered cerebral perfusion (67, 68), all of which can reduce tracer delivery. Consistent with this, we observed a widespread decreasing trend in the K_1 values of [^{18}F]SynVesT-1 across the brain in EAE mice, although this reduction reached statistical significance only in specific regions (*SI Appendix*, Fig. S4). While the total V_T theoretically corrects for alterations in tracer delivery, severe perfusion deficits can introduce noise into kinetic modeling, particularly in small animals where achieving a perfect model fit is challenging. Be that as it may, the fact that V_T was significantly reduced across all analyzed regions, regardless of whether

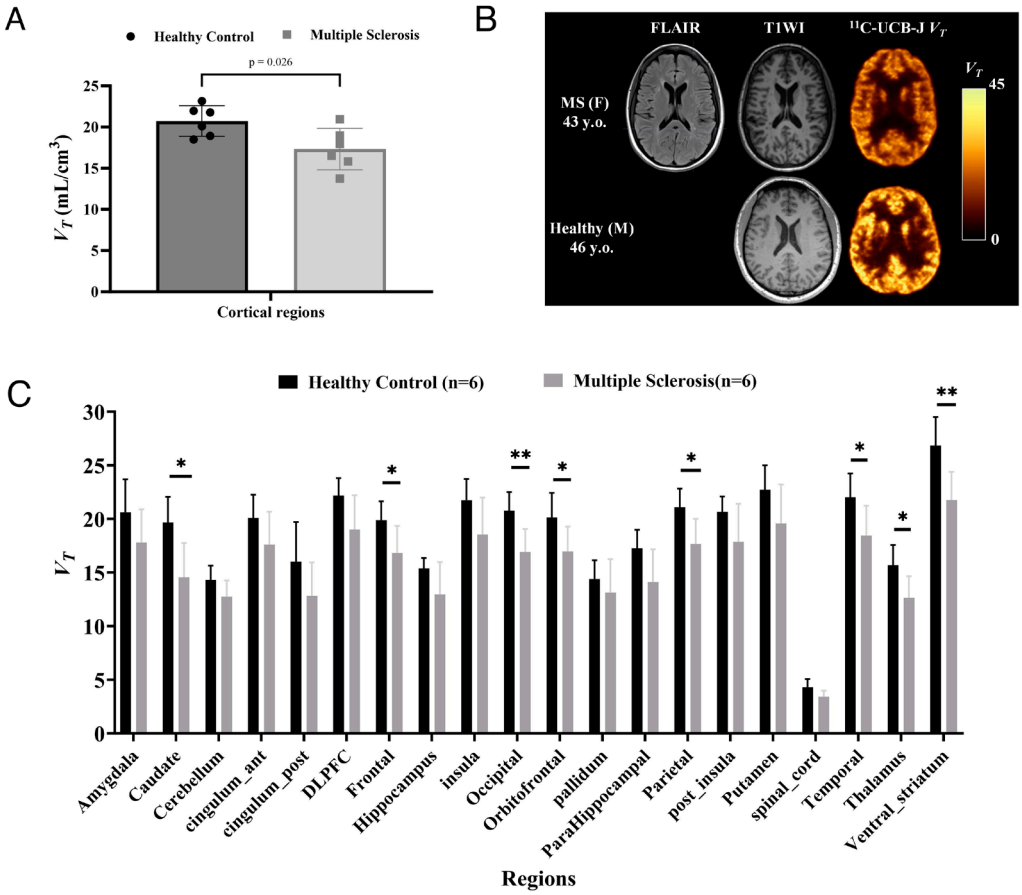

Fig. 6. [^{11}C]UCB-J PET reveals decreased SV2A tracer uptake in MS. (*A*) Comparison of [^{11}C]UCB-J binding in the cortical regions between people with MS and HCs. (*B*) Illustration of the difference in total brain [^{11}C]UCB-J uptake between an MS participant and a HC. The top row shows the MRI (FLAIR and T1-weighted) and [^{11}C]UCB-J V_T parametric PET image of a female MS participant. The bottom row displays the corresponding MRI and [^{11}C]UCB-J V_T parametric PET image of a similarly aged HC. (*C*) Comparison of [^{11}C]UCB-J bindings in different brain regions between people with MS and HCs. Data are presented as mean ± SD. *$P \leq 0.05$, **$P \leq 0.005$.

K_1 reached significance, suggests that the observed decline in synaptic density is not driven solely by deficits in tracer delivery. In the pilot human cohort, no significant difference between groups in K_1 was observed. Taken together, these considerations indicate that BBB and perfusion alterations remain potential confounds and limitations of the present study, but are unlikely to fully account for the magnitude or spatial pattern of the SV2A reductions.

To address the concern that the observed reduction in V_T might be driven primarily by perfusion deficits rather than genuine synaptic loss, we undertook several validation studies. First, we confirmed radiotracer specificity in vivo via a blocking study (*SI Appendix*, Fig. S1): LEV effectively displaced [^{18}F]SynVesT-1 in both the brain and spinal cord, demonstrating that the PET signal reflects specific SV2A binding even in the context of neuroinflammation. Having established specificity of the SV2A signal, we then examined the robustness of our primary finding across quantification methods. The reduction in tracer binding was consistent across all quantification metrics including V_T and SUVR, indicating that the main biological signal is preserved irrespective of input function choice or pseudoreference assumptions. Nonetheless, high intrasubject correlations across major brain regions (*SI Appendix*, Fig. S9) further suggest a global, diffuse pattern of synaptic pathology in the EAE mice. We further corroborated the PET findings with complementary ARG and histological assays. Ex vivo ARG at the whole-brain level confirmed the in vivo distribution and retention of [^{18}F]SynVesT-1 (*SI Appendix*, Fig. S7), supporting the specificity of the PET signal. In vitro ARG demonstrated that [^{18}F]SynVesT-1 binding was predominantly specific to SV2A and could be blocked by LEV in EAE mouse brain tissue (60), consistent with the in vivo blocking results (Fig. 5*A* and *SI Appendix*, Fig. S5*B*). Although the decrease in hippocampal binding in in vitro ARG did not reach statistical significance, this likely reflects the smaller sample size in this subset and the impact of differences in tracer kinetics between in vivo PET and in vitro binding assays, as has been noted for other radiotracers (69). Previous histological studies in EAE have already documented substantial loss of pre- and postsynaptic markers, indicating robust synaptic pathology in this model (64, 70, 71). In the present study, SV2A IF staining revealed regionally reduced SV2A protein expression that qualitatively paralleled the regional PET findings (*SI Appendix*, Fig. S6), supporting the interpretation that [^{18}F]SynVesT-1 signal reduction primarily reflects lower SV2A protein availability rather than a purely kinetic or modeling artifact. Nonetheless, given the relatively small sample size of the ex vivo cohort, these histological findings should be considered corroborative, and larger studies are warranted to fully characterize regional heterogeneity of SV2A expression.

Given that SV2A PET tracers have recently been applied as noninvasive tools to image spinal cord damage in rodents across several disease contexts (50, 53, 72), we also evaluated [^{18}F]SynVesT-1 PET imaging in the EAE spinal cord. Interestingly, although the PET signal was significantly blocked in the cervical, thoracic,

and lumbar sections, the sacral region showed predominantly nonspecific binding (*SI Appendix*, Fig. S1 *A*, *C*, and *E*). This is likely due to the partial volume effect (PVE) and the reduced level of SV2A protein along the spinal cord axis. Regarding quantification, as expected, the uptake of tracers in the spinal cord regions was generally lower than in the cerebral regions, where we found a two- and threefold difference between naïve and EAE mice, in agreement with previous reports (72, 73). Based on the nonspecific binding profile observed in the sacral region, we used it as a reference tissue to calculate both SUVR and DVR. Both metrics consistently revealed a significant reduction in tracer uptake in the cervical and lumbar segments, aligning with previous reports of synaptic loss in the EAE spinal cord (74). In addition, in vitro ARG and IF staining in spinal cord regions showed regional patterns of SV2A reduction that corroborated the in vivo PET findings, further supporting that the [^{18}F]SynVesT-1 signal predominantly reflects changes in SV2A expression rather than methodological or kinetic artifacts (Fig. 5 *C* and *D* and *SI Appendix*, Fig. S6 *C* and *D*). Note that, however, ex vivo ARG of spinal cord segments was not performed, as the short half-life of [^{18}F]SynVesT-1 combined with the small size of the mouse spinal cord imposes substantial practical constraints on rapid tissue processing and high-resolution quantitative imaging within the available time window. Surprisingly, we did not observe significant differences in the thoracic segment, which is also shown in our in vitro data, although there is still a clear decreasing trend of SV2A protein expression in vitro. This finding likely reflects the distinct anatomical composition and disease heterogeneity of the spinal segments. In fact, the low gray-to-white matter ratio in the thoracic region inherently limits the sensitivity of quantification assays, making the detection of synaptic changes more challenging compared to the gray-matter-rich enlargements (75, 76). Given these anatomical complexities and the limited sample size of our validation cohort, we cannot definitively rule out subtle pathology in this region. Thus, future studies with larger sample sizes are warranted to confirm the extent of thoracic pathology.

Meanwhile, to provide translational validation for our preclinical findings, we conducted a proof-of-concept SV2A PET imaging in human MS patients using [^{11}C]UCB-J, the first and widely validated radiotracer that serves as the clinical benchmark for SV2A quantification (54, 55). Although different tracers were employed for mice and humans in this study, both [^{11}C]UCB-J and [^{18}F]SynVesT-1 are excellent SV2A tracers with similar binding characteristics (48, 77). The choice between these tracers is largely dictated by institutional availability. While [^{11}C]UCB-J is the first and most extensively validated SV2A PET tracer in humans, [^{18}F]SynVesT-1 was developed more recently and was not yet available for clinical use at the time this study was conducted. The primary findings indicated a widespread loss of SV2A and synaptic density, with a statistically significant 16.6% reduction in [^{11}C]UCB-J binding in the cortical regions of MS participants compared to healthy controls. Importantly, these observations are consistent with recent emerging reports demonstrating SV2A reduction in independent MS cohorts (51). Notably, this decreasing trend in SV2A binding was observed across all analyzed brain regions and the spinal cord, underscoring the pervasive nature of synaptic degradation in MS and the ability of SV2A PET imaging in capturing synaptic density loss in MS patients. Some regions, such as the caudate and frontal cortex, reached statistical significance, highlighting areas of particularly pronounced synaptic loss. Although our study did not specifically match participants by sex, previous research suggests no significant sex differences in [^{11}C]UCB-J binding (78, 79). This finding supports the generalizability of our results across both sexes, particularly regarding the small cohort of this human study. In human data analysis, we did not employ image-based reference methods. This choice reflects the diffuse nature of MS-related pathology, which can affect both white and gray matter throughout the brain and spinal cord. As a result, no brain region can be reliably assumed to be unaffected and therefore suitable as a reference region for normalization.

From a translational standpoint, our data indicate that SV2A PET is sufficiently sensitive to detect robust synaptic loss at peak disease in EAE (≈25 to 30% reductions in V_T across multiple brain regions and segment-specific decreases in the spinal cord) and moderate cortical synaptic loss in MS patients (≈17% reduction in [^{11}C]UCB-J binding). However, the sensitivity of this approach for monitoring subtler changes associated with early disease, gradual progression, or partial therapeutic rescue remains to be defined. In fact, these findings must be interpreted in light of several limitations. First, while the resolution of preclinical PET scanners allowed for the distinction of spinal cord segments, the small cross-sectional area of the mouse spinal cord creates inherent challenges regarding PVE (80, 81). Although we employed a reference region strategy to mitigate this, future studies utilizing higher-resolution modalities or PVE-correction algorithms could further refine quantification in the thoracic and sacral segments. Moreover, small animal size, PVE, and disease-related perfusion alterations may limit the detectability of small longitudinal changes, underscoring the need for optimized acquisition protocols, higher-resolution imaging, and adequately powered longitudinal treatment studies. In the clinical setting, test–retest variability, interindividual differences, and practical constraints on repeated PET scanning will similarly constrain the minimal detectable change and thus the utility of SV2A PET as a progression or treatment-response biomarker. Second, the kinetic modeling in the preclinical model of MS relied on a population-based radiometabolite correction. While a series of analysis indicates that the observed reduction in SV2A binding is robust to this assumption, the lack of subject-specific metabolic profiles prevents the complete exclusion of metabolic confounds. Future work should therefore aim to incorporate detailed radiometabolite characterization to further precision-map these kinetic parameters. Finally, the current study is cross-sectional and focuses on establishing the magnitude of synaptic loss at peak disease. Multi–time point cohorts in both EAE and MS will be required to formally determine effect sizes, minimal detectable changes, and the time window over which SV2A PET can most effectively track disease trajectory and therapeutic efficacy.

There has been growing therapeutic effort aimed at restoring synaptic density loss in MS (8, 82, 83). Considering the widespread reduction of synaptic density in MS, the use of noninvasive imaging like SV2A PET, which is distributed across the brain and gray matter, will offer crucial insights into evaluating these novel neuroprotective strategies. By bridging the gap between preclinical findings and clinical application, this imaging approach holds significant potential for directing future therapeutic interventions and objectively monitoring synaptic health in MS.

Conclusion

Using PET imaging in EAE mice and in a pilot cohort of patients with MS, we successfully detected significant reductions of SV2A in MS and related animal models. Our findings demonstrate that SV2A PET can reliably quantify presynaptic alterations in vivo in a preclinical MS model and a clinical research study. The observed tracer uptake patterns emphasize the potential of SV2A PET for

detecting widespread synaptic pathology and for supporting mechanistic and therapeutic studies in MS.

Data, Materials, and Software Availability. All study data are included in the article and/or *SI Appendix*. No code or sequencing data were generated.

ACKNOWLEDGMENTS. We gratefully acknowledge the Canadian Institutes of Health Research (CIHR507113 and CIHR551424, C.Z.), Nancy Davis Foundation, Alzheimer's Association, Michael J. Fox Foundation, and Weston Brain Institute for financial support (MJFF-007878). N.V. thanks the Azrieli Foundation, Canada Foundation for Innovation, Ontario Research Fund, and the Canada Research Chairs Program for support.

Author affiliations: [a]Azrieli Centre for Neuro-Radiochemistry, Brain Health Imaging Centre, Campbell Family Mental Health Research Institute, Centre for Addiction and Mental Health, Toronto, ON M5T 1R8, Canada; [b]Department of Pharmacology and Toxicology, Temerty Faculty of Medicine, University of Toronto, Toronto, ON M5G 2C8, Canada; [c]Department of Radiology and Biomedical Imaging, Yale School of Medicine, Yale University, New Haven, CT 06520; [d]Department of Psychiatry, Temerty Faculty of Medicine, University of Toronto, Toronto, ON M5T 1R8, Canada; [e]Department of Neurology, Yale School of Medicine, Yale University, New Haven, CT 06520; [f]Neurocenter, Turku University Hospital, University of Turku, Turku 20521, Finland; and [g]Department of Chemistry, University of Toronto, Toronto, ON M5S 3H6, Canada

Author contributions: P.H.J.C., M.-K.C., and C.Z. designed research; P.H.J.C., T.T., J.T., H.L., M.D., L.A., M.-K.C., and C.Z. performed research; T.T., J.T., A.J.B., R.R., E.E.L., Y.H., R.E.C., N.V., and C.Z. contributed new reagents/analytic tools; P.H.J.C., T.T., J.T., M.-K.C., and C.Z. analyzed data; N.V., M.-K.C., and C.Z. funding support; and P.H.J.C., T.T., M.-K.C., and C.Z. wrote the paper.

1. P. K. Stys, Axonal degeneration in multiple sclerosis: Is it time for neuroprotective strategies? *Ann. Neurol.* **55**, 601–603 (2004).
2. P. K. Stys *et al.*, New views on the complex interplay between degeneration and autoimmunity in multiple sclerosis. *Front. Cell. Neurosci.* **18**, 1426231 (2024).
3. A. Thompson, O. Ciccarelli, Towards treating progressive multiple sclerosis. *Nat. Rev. Neurol.* **16**, 589–590 (2020).
4. B. Bodini, M. Tonietto, L. Airas, B. Stankoff, Positron emission tomography in multiple sclerosis–Straight to the target. *Nat. Rev. Neurol.* **17**, 663–675 (2021).
5. S. Espírito-Santo, V. G. Coutinho, F. C. Alcantara Gomes, Synaptic pathology in multiple sclerosis: A role for Nogo-A signaling in astrocytes?. *Neural Regen. Res.* **18**, 127–128 (2023).
6. M. Filippi *et al.*, Multiple sclerosis. *Nat. Rev. Dis. Primers* **4**, 1–27 (2018).
7. V. G. Coutinho Costa, S.E.-S. Araújo, S. V. Alves-Leon, F. C. A. Gomes, Central nervous system demyelinating diseases: Glial cells at the hub of pathology. *Front. Immunol.* **14**, 1135540 (2023).
8. L. Bellingacci *et al.*, Synaptic dysfunction in multiple sclerosis: A red thread from inflammation to network disconnection. *Int. J. Mol. Sci.* **22**, 9753 (2021).
9. M. Di Filippo, E. Portaccio, A. Mancini, P. Calabresi, Multiple sclerosis and cognition: Synaptic failure and network dysfunction. *Nat. Rev. Neurosci.* **19**, 599–609 (2018).
10. G. Mandolesi *et al.*, Synaptopathy connects inflammation and neurodegeneration in multiple sclerosis. *Nat. Rev. Neurol.* **11**, 711–724 (2015).
11. A. Compston, A. Coles, Multiple sclerosis. *Lancet* **372**, 1502–1517 (2008).
12. S. A. Liddelow *et al.*, Neurotoxic reactive astrocytes are induced by activated microglia. *Nature* **541**, 481–487 (2017).
13. J. M. Frischer *et al.*, The relation between inflammation and neurodegeneration in multiple sclerosis brains. *Brain* **132**, 1175–1189 (2009).
14. B. D. Trapp, K.-A. Nave, Multiple sclerosis: An immune or neurodegenerative disorder? *Annu. Rev. Neurosci.* **31**, 247–269 (2008).
15. C. S. Constantinescu, N. Farooqi, K. O'Brien, B. Gran, Experimental autoimmune encephalomyelitis (EAE) as a model for multiple sclerosis (MS). *Br. J. Pharmacol.* **164**, 1079–1106 (2011).
16. R. M. Ransohoff, Animal models of multiple sclerosis: The good, the bad and the bottom line. *Nat. Neurosci.* **15**, 1074–1077 (2012).
17. R. L. Gillani, E. N. Kironde, S. Whiteman, T. J. Zwang, B. J. Bacskai, Instability of excitatory synapses in experimental autoimmune encephalomyelitis and the outcome for excitatory circuit inputs to individual cortical neurons. *Brain. Behav. Immun.* **119**, 251–260 (2024).
18. N. Petrova *et al.*, Synaptic loss in multiple sclerosis spinal cord. *Ann. Neurol.* **88**, 619–625 (2020).
19. M. Albert *et al.*, Synaptic pathology in the cerebellar dentate nucleus in chronic multiple sclerosis. *Brain Pathol. Zurich Switz.* **27**, 737–747 (2017).
20. M. E. Serrano, E. Kim, M. M. Petrinovic, F. Turkheimer, D. Cash, Imaging synaptic density: The next holy grail of neuroscience?. *Front. Neurosci.* **16**, 796129 (2022).
21. Z. Cai, S. Li, D. Matuskey, N. Nabulsi, Y. Huang, PET imaging of synaptic density: A new tool for investigation of neuropsychiatric diseases. *Neurosci. Lett.* **691**, 44–50 (2019).
22. M. A. Friese, Widespread synaptic loss in multiple sclerosis. *Brain* **139**, 2–4 (2016).
23. C. Cordano *et al.*, Synaptic injury in the inner plexiform layer of the retina is associated with progression in multiple sclerosis. *Cell Rep. Med.* **5**, 101490 (2024).
24. J.-M. Tillema, I. Pirko, Neuroradiological evaluation of demyelinating disease. *Ther. Adv. Neurol. Disord.* **6**, 249–268 (2013).
25. Y. Miki, Magnetic resonance imaging diagnosis of demyelinating diseases: An update. *Clin. Exp. Neuroimmunol.* **10**, 32–48 (2019).
26. M.-K. Chen *et al.*, Assessing synaptic density in Alzheimer disease with synaptic vesicle glycoprotein 2A positron emission tomographic imaging. *JAMA Neurol.* **75**, 1215–1224 (2018).
27. M. Malpetti *et al.*, Synaptic loss in frontotemporal dementia revealed by [11C]UCB-J positron emission tomography. *Ann. Neurol.* **93**, 142–154 (2023).
28. E. M. Ullrich Gavilanes *et al.*, SV2A-PET imaging uncovers cortical synapse loss in multiple sclerosis. *Sci. Transl. Med.* **17**, eadt5585 (2025).
29. E. Tavazzi *et al.*, MRI biomarkers of disease progression and conversion to secondary-progressive multiple sclerosis. *Expert Rev. Neurother.* **20**, 821–834 (2020).
30. M. L. James, S. S. Gambhir, A molecular imaging primer: Modalities, imaging agents, and applications. *Physiol. Rev.* **92**, 897–965 (2012).
31. M. E. Phelps, Positron emission tomography provides molecular imaging of biological processes. *Proc. Natl. Acad. Sci.* **97**, 9226–9233 (2000).
32. P. M. Matthews, E. A. Rabiner, J. Passchier, R. N. Gunn, Positron emission tomography molecular imaging for drug development. *Br. J. Clin. Pharmacol.* **73**, 175–186 (2012).
33. W. Wei *et al.*, Predicting PET-derived myelin content from multisequence MRI for individual longitudinal analysis in multiple sclerosis. *Neuroimage* **223**, 117308 (2020).
34. M. Veronese *et al.*, Quantification of [11C]PIB PET for imaging myelin in the human brain: A test–retest reproducibility study in high-resolution research tomography. *J. Cereb. Blood Flow Metab.* **35**, 1771–1782 (2015).
35. S. M. Bajjalieh, G. D. Frantz, J. M. Weimann, S. K. McConnell, R. H. Scheller, Differential expression of synaptic vesicle protein 2 (SV2) isoforms. *J. Neurosci. Off. J. Soc. Neurosci.* **14**, 5223–5235 (1994).
36. S. J. Finnema *et al.*, Imaging synaptic density in the living human brain. *Sci. Transl. Med.* **8**, 348ra96 (2016).
37. S. E. Holmes *et al.*, Lower synaptic density is associated with depression severity and network alterations. *Nat. Commun.* **10**, 1529 (2019).
38. N. B. Nabulsi *et al.*, Synthesis and preclinical evaluation of 11C-UCB-J as a PET tracer for imaging the synaptic vesicle glycoprotein 2A in the brain. *J. Nucl. Med.* **57**, 777–784 (2016).
39. S. Estrada *et al.*, [(11)C]UCB-A, a novel PET tracer for synaptic vesicle protein 2A. *Nucl. Med. Biol.* **43**, 325–332 (2016).
40. G. I. Warnock *et al.*, Evaluation of 18F-UCB-H as a novel PET tracer for synaptic vesicle protein 2A in the brain. *J. Nucl. Med.* **55**, 1336–1341 (2014).
41. F. Bretin *et al.*, Biodistribution and radiation dosimetry for the novel SV2A radiotracer [18F]UCB-H: First-in-human study. *Mol. Imaging Biol.* **17**, 557–564 (2015).
42. S. Li *et al.*, Synthesis and in vivo evaluation of a novel PET radiotracer for imaging of synaptic vesicle glycoprotein 2A (SV2A) in nonhuman primates. *ACS Chem. Neurosci.* **10**, 1544–1554 (2019).
43. Z. Cai *et al.*, Synthesis and preclinical evaluation of an ^{18}F-labeled synaptic vesicle glycoprotein 2A PET imaging probe: [^{18}F]SynVesT-2. *ACS Chem. Neurosci.* **11**, 592–603 (2020).
44. L. R. Drake *et al.*, First-in-human study of 18F-SynVesT-2: An SV2A PET imaging probe with fast brain kinetics and high specific binding. *J. Nucl. Med.* **65**, 462–469 (2024).
45. C. Zheng *et al.*, A metabolically stable PET tracer for imaging synaptic vesicle protein 2A: Synthesis and preclinical characterization of [18F]SDM-16. *Eur. J. Nucl. Med. Mol. Imaging* **49**, 1482–1496 (2022).
46. C. Zheng *et al.*, Decreased synaptic vesicle glycoprotein 2A binding in a rodent model of familial Alzheimer's disease detected by [18F]SDM-16. *Front. Neurol.* **14**, 1045644 (2023).
47. S. L. Martin, C. Uribe, A. P. Strafella, PET imaging of synaptic density in Parkinsonian disorders. *J. Neurosci. Res.* **102**, e25253 (2024).
48. M. Naganawa *et al.*, First-in-human evaluation of ^{18}F-SynVesT-1, a radioligand for PET imaging of synaptic vesicle glycoprotein 2A. *J. Nucl. Med.* **62**, 561–567 (2021).
49. C. Zheng *et al.*, [18F]Synvest-1 PET detects synaptic changes in a rat model of disease. *J. Nucl. Med.* **65**, 241593–241593 (2024).
50. B. Chen *et al.*, [18F]SynVesT-1 PET detects SV2A changes in the spinal cord and brain of rats with spinal cord injury. *J. Nucl. Med.* **66**, 1440–1448 (2025).
51. A. Luoma *et al.*, Synaptic density in multiple sclerosis. *Neurol. Neuroimmunol. Neuroinflamm.* **12**, e200435 (2025).
52. J. H. Kim *et al.*, Detecting axon damage in spinal cord from a mouse model of multiple sclerosis. *Neurobiol. Dis.* **21**, 626–632 (2006).
53. D. Bertoglio *et al.*, SV2A PET imaging is a noninvasive marker for the detection of spinal damage in experimental models of spinal cord injury. *J. Nucl. Med.* **63**, 1245–1251 (2022).
54. N. B. Nabulsi *et al.*, Synthesis and preclinical evaluation of 11C-UCB-J as a PET tracer for imaging the synaptic vesicle glycoprotein 2A in the brain. *J. Nucl. Med.* **57**, 777–784 (2016).
55. G. Becker, S. Dammicco, M. A. Bahri, E. Salmon, The rise of synaptic density PET imaging. *Mol. Basel Switz.* **25**, 2303 (2020).
56. K. L. Desmond *et al.*, First-in-human PET imaging of [18F]SDM-4MP3: A cautionary tale. *Mol. Imaging* **2023**, 8826977 (2023).
57. A. E. Dorr, J. P. Lerch, S. Spring, N. Kabani, R. M. Henkelman, High resolution three-dimensional brain atlas using an average magnetic resonance image of 40 adult C57Bl/6J mice. *Neuroimage* **42**, 60–69 (2008).
58. M. Harrison *et al.*, Vertebral landmarks for the identification of spinal cord segments in the mouse. *Neuroimage* **68**, 22–29 (2013).
59. D. Bertoglio *et al.*, Validation, kinetic modeling, and test-retest reproducibility of [18F]SynVesT-1 for PET imaging of synaptic vesicle glycoprotein 2A in mice. *J. Cereb. Blood Flow Metab. Off. J. Int. Soc. Cereb. Blood Flow Metab.* **42**, 1867–1878 (2022).
60. B. A. Lynch *et al.*, The synaptic vesicle protein SV2A is the binding site for the antiepileptic drug levetiracetam. *Proc. Natl. Acad. Sci. U.S.A.* **101**, 9861–9866 (2004).
61. S. J. Finnema *et al.*, Kinetic evaluation and test-retest reproducibility of [11C]UCB-J, a novel radioligand for positron emission tomography imaging of synaptic vesicle glycoprotein 2A in humans. *J. Cereb. Blood Flow Metab. Off. J. Int. Soc. Cereb. Blood Flow Metab.* **38**, 2041–2052 (2018).
62. A. P. Mecca *et al.*, In vivo measurement of widespread synaptic loss in Alzheimer's disease with SV2A PET. *Alzheimers Dement. J. Alzheimers Assoc.* **16**, 974–982 (2020).
63. E. E. A. Möck, E. Honkonen, L. Airas, Synaptic loss in multiple sclerosis: A systematic review of human post-mortem studies. *Front. Neurol.* **12**, 782599 (2021).
64. M. O. Ziehn, A. A. Avedisian, S. Tiwari-Woodruff, R. R. Voskuhl, Hippocampal CA1 atrophy and synaptic loss during experimental autoimmune encephalomyelitis, EAE. *Lab. Investig. J. Tech. Methods Pathol.* **90**, 774–786 (2010).
65. A. Miranda, D. Bertoglio, C. De Weerdt, S. Staelens, J. Verhaeghe, Isoflurane and ketamine-xylazine modify pharmacokinetics of [^{18}F]SynVesT-1 in the mouse brain. *J. Cereb. Blood Flow Metab.* **43**, 1612–1624 (2023).
66. M. Xiong *et al.*, Synaptic density in aging mice measured by [18F]SynVesT-1 PET. *Neuroimage* **277**, 120230 (2023).
67. B. Engelhardt *et al.*, Vascular, glial, and lymphatic immune gateways of the central nervous system. *Acta Neuropathol. (Berl.)* **132**, 317–338 (2016).

68. R. Lin *et al.*, Depleting parenchymal border macrophages alleviates cerebral edema and neuroinflammation following status epilepticus. *J. Transl. Med.* **22**, 1094 (2024).
69. H. Toyama *et al.*, [18F]fdg mouse brain PET imaging: Absolute quantification of regional cerebral glucose utilization as compared with 2-[14C]dg autoradiography. *Int. Congr. Ser.* **1265**, 255–261 (2004).
70. S. Werneburg *et al.*, Targeted complement inhibition at synapses prevents microglial synaptic engulfment and synapse loss in demyelinating disease. *Immunity* **52**, 167–182.e7 (2020).
71. A. M. Hamilton *et al.*, Central nervous system targeted autoimmunity causes regional atrophy: A 9.4T MRI study of the EAE mouse model of multiple sclerosis. *Sci. Rep.* **9**, 8488 (2019).
72. D. Bertoglio *et al.*, Synaptic vesicle glycoprotein 2a is affected in the central nervous system of mice with Huntington disease and in the brain of a human with Huntington disease postmortem. *J. Nucl. Med.* **63**, 942–947 (2022).
73. N. Lambeng, M. Gillard, P. Vertongen, B. Fuks, P. Chatelain, Characterization of [3H]ucb 30889 binding to synaptic vesicle protein 2A in the rat spinal cord. *Eur. J. Pharmacol.* **520**, 70–76 (2005).
74. L. Xin *et al.*, Impairment of spinal CSF flow precedes immune cell infiltration in an active EAE model. *J. Neuroinflammation* **21**, 272 (2024).
75. P. W. Stroman *et al.*, The current state-of-the-art of spinal cord imaging: Methods. *Neuroimage* **84**, 1070–1081 (2014).
76. M. Bilgen, Magnetic resonance microscopy of spinal cord injury in mouse using a miniaturized implantable RF coil. *J. Neurosci. Methods* **159**, 93–97 (2007).
77. R. H. Asch *et al.*, Evaluating infusion methods and simplified quantification of synaptic density *in vivo* with [11C]UCB-J and [18F]SynVesT-1 PET. *J. Cereb. Blood Flow Metab.* **43**, 2120–2129 (2023).
78. L. Michiels *et al.*, Synaptic density in healthy human aging is not influenced by age or sex: A 11C-UCB-J PET study. *Neuroimage* **232**, 117877 (2021).
79. T. Toyonaga *et al.*, The regional pattern of age-related synaptic loss in the human brain differs from gray matter volume loss: In vivo PET measurement with [11C]UCB-J. *Eur. J. Nucl. Med. Mol. Imaging* **51**, 1012–1022 (2024).
80. P. Kanel, G. Carli, R. Vangel, S. Roytman, N. I. Bohnen, Challenges and innovations in brain PET analysis of neurodegenerative disorders: A mini-review on partial volume effects, small brain region studies, and reference region selection. *Front. Neurosci.* **17**, 1293847 (2023).
81. M. Soret, S. L. Bacharach, I. Buvat, Partial-volume effect in PET tumor imaging. *J. Nucl. Med.* **48**, 932–945 (2007).
82. D. Zhai *et al.*, Small-molecule targeting AMPA-mediated excitotoxicity has therapeutic effects in mouse models for multiple sclerosis. *Sci. Adv.* **9**, eadj6187 (2023).
83. M. M. Poon *et al.*, Targeting the muscarinic M1 receptor with a selective, brain-penetrant antagonist to promote remyelination in multiple sclerosis. *Proc. Natl. Acad. Sci. U.S.A.* **121**, e2407974121 (2024).